



This is a repository copy of *In-situ synchrotron imaging of keyhole mode multi-layer laser powder bed fusion additive manufacturing*.

White Rose Research Online URL for this paper:
<https://eprints.whiterose.ac.uk/160634/>

Version: Accepted Version

Article:

Chen, Y., Clark, S.J., Leung, C.L.A.. et al. (7 more authors) (2020) In-situ synchrotron imaging of keyhole mode multi-layer laser powder bed fusion additive manufacturing. *Applied Materials Today*, 20. 100650. ISSN 2352-9407

<https://doi.org/10.1016/j.apmt.2020.100650>

Article available under the terms of the CC-BY-NC-ND licence
(<https://creativecommons.org/licenses/by-nc-nd/4.0/>).

Reuse

This article is distributed under the terms of the Creative Commons Attribution-NonCommercial-NoDerivs (CC BY-NC-ND) licence. This licence only allows you to download this work and share it with others as long as you credit the authors, but you can't change the article in any way or use it commercially. More information and the full terms of the licence here: <https://creativecommons.org/licenses/>

Takedown

If you consider content in White Rose Research Online to be in breach of UK law, please notify us by emailing eprints@whiterose.ac.uk including the URL of the record and the reason for the withdrawal request.



eprints@whiterose.ac.uk
<https://eprints.whiterose.ac.uk/>

Synchrotron Imaging of Keyhole Mode Multi-layer Laser Powder Bed Fusion Additive Manufacturing

*Yunhui Chen^{1,2}, Samuel J. Clark^{1,2}, Chu-Lun Alex Leung^{1,2}, Lorna Sinclair^{1,2}, Sebastian Marussi^{1,2}, Margie P. Olbinado³, Elodie Boller³, Alexander Rack³, Iain Todd⁴, *Peter D. Lee^{1,2}

¹ UCL Mechanical Engineering, University College London, Torrington Place, London WC1E 7JE, UK

² Research Complex at Harwell, Rutherford Appleton Laboratory, Oxfordshire OX11 0FA, UK

³ ESRF – The European Synchrotron, Grenoble, 38043 Cedex 9, France

⁴ Department of Materials Science and Engineering, University of Sheffield, Sir Robert Hadfield Building, Mappin Street, Sheffield, S1 3JD, UK

Abstract

The keyhole mode in laser powder bed fusion (LPBF) additive manufacturing can be associated with excessive porosity and spatter, however, the underlying physics in multilayer build conditions remain unclear. Here, we used ultra-fast synchrotron X-ray imaging to reveal this phenomena. We revealed melt pool dynamics, keyhole porosity and spatter formation mechanisms and their impact in all layers of the build. We observed that the transient melt pool dynamics associated with the keyhole include: (I) keyhole initiation, (II) keyhole development, and (III) melt pool recovery. Porosity and spatter were associated with stages (II) and (III). We also discovered that droplet spatter can form due to the collapse of the keyhole recoil zone, causing molten particle agglomeration and ejection during stage (III). Our results clarify the transient dynamics behind the keyhole mode in a multi-layer LBPF process and can be used to guide the reduction in porosity and spatter in additive manufacturing. (150 words)

Keywords: Additive manufacturing, laser powder bed fusion; keyhole mode; synchrotron X-ray imaging

*Corresponding author: peter.lee@ucl.ac.uk, yunhui.chen@ucl.ac.uk

1. Introduction

Laser additive manufacturing (LAM), such as laser powder bed fusion (LPBF), is a key enabling technology that facilitates the fabrication of components with complex shapes directly from digital designs, layer by layer. LPBF is among the most promising methods in LAM due to its high accuracy¹. The technique has been adopted in aerospace^{2,3}, biomedical^{4,5} and energy storage^{6,7} applications. However, the utilisation of LPBF for the manufacture of safety critical metallic components is hindered by technical challenges during processing which can lead to the formation of porosity, lack of fusion and cracking in the final part. Those features have a detrimental effect on the mechanical properties such as static strength, fracture toughness and resistance to failure by fatigue during cyclic loading. Porosity formation during melting and re-solidification of tracks in the powder bed, as successive layers are built, is one of the principal features that leads to reduced properties. In LPBF, the spatter, which is the ejection of particles from the melt pool during melting of powder materials, is a detrimental by-product which can contaminate the powder bed and/or adhere to the solidified track surface and increase the surface roughness. Both of these phenomena potentially increase the probability of porosity formation^{8,9} in subsequent layer additions and so spatter formation¹⁰ is a significant issue. It is therefore essential to gain an enhanced understanding of, and ability to prevent, porosity and spatter formation in order to realise the goal of industrialised production of safety critical LAM components.

Depending on laser energy density, a crucial indicator of energy input associated with laser power and scan speed, the laser-matter interaction may exhibit conduction mode or keyhole mode¹¹ melting during LPBF. If the energy input exceeds a certain criteria¹², LPBF is operated in keyhole mode when the power density of the laser beam is sufficient to generate metal evaporation. It is featured by a vapour cavity that enhances the laser absorption. The keyhole mode laser melting is frequently employed in LPBF as it allows the laser energy to transfer more efficiently to the powder layer by incorporating multiple reflections of the laser in the vapour cavity of the keyhole¹³. Consequently, the laser-matter interaction is very complex due to strong vaporisation of material from the molten pool and the flow of molten metal in the keyhole, driven by recoil pressure and Marangoni convection¹⁴. Whilst there are clear benefits to the use of keyhole mode conditions in LPBF, it often leads to excessive porosity¹⁴ and spatter¹⁵ if processing parameters are not properly controlled.

52 Therefore, it is critical to understand the mechanisms of porosity formation and spatter generation associated
53 with the keyhole mode in order to optimise the integrity of components built by LPBF.

54 Recently, much research, including high speed imaging of the operation of LPBF, microstructural
55 characterisation of built parts and computational modelling of the process has been performed to attempt to
56 better understand keyhole and spatter phenomena^{16,17}. In situ and operando high-speed X-ray radiography
57 investigations have been proven to capture the transient phenomena in a range of processes, including
58 LPBF^{18,19}. Third-generation synchrotron radiation sources^{20,21} enable high intensity X-rays to penetrate
59 through a sufficient thickness of a metallic sample with ultra-high temporal (tenths of microseconds) and
60 spatial (a few micro- metres) resolution. In LAM, synchrotron in situ research has focussed predominantly on
61 single powder layer conditions in the experimental design to visualise the keyhole morphology²² and the gas-
62 liquid interface fluctuation²³ of the keyhole wall in a substrate plate. Additionally, pore circulation and
63 elimination by thermocapillary force²⁴ and during hatching²⁵ has also been explored. A pore mitigation
64 strategy was proposed to prevent pore formation by modulating laser power in keyhole mode with powder
65 density of $\sim 10.2 \text{ MW cm}^{-2}$ ²⁵. While powder spatter is reported to be induced by the metal vapour jet/plume²⁶,
66 laser absorption of powders and the role of powders and previous layers in multi-layer conditions were not
67 addressed. Keyhole mode melt pool dynamics and its relation to both porosity and spatter formation
68 mechanisms, especially in multi-layer conditions, are thus still unclear. Materials including stainless steel¹⁰,
69 bio-glass¹⁹ and AISi10Mg²⁴ have been explored in situ for their behaviour under laser irradiation. However,
70 spatter formation in Ti-6Al-4V, which is a key material for aerospace and biomedical applications, has only
71 been investigated in the bulk material.²⁷

72 In the present work, we perform in situ and operando synchrotron X-ray radiography of LPBF in a five-layer
73 build condition on a solid substrate, with 100 μm powder layer thickness on each layer. Our aim is to
74 investigate the melt pool dynamics of the keyhole mode and its relationship with porosity and spatter
75 formation mechanisms in Ti-6Al-4V. We reveal the melt pool dynamics which is a cyclic event with a transient
76 separation of the portion of the melt pool in front of the laser. We elucidate how this cyclical process is related
77 both to the generation of keyhole porosity and spatter formation in every layer of a build. The results
78 presented in this work provide an enhanced understanding of LPBF AM which is directly relevant to multilayer
79 powder bed printing of parts. The mechanisms observed are potentially applicable to other laser materials
80 processing techniques such as directed energy deposition and laser welding.

2. Materials & Methods

2.1 *In situ* and operando synchrotron X-ray imaging

In situ and operando X-ray imaging on the ID19 beamline at the European Synchrotron Radiation Facility (ESRF) was performed to capture the melt pool and transient porosity and spatter dynamics in this study. The LAM process replicator, the In Situ and Operando Powder bed process Replicator (ISOPR), which mimics a commercial L-PBF system was developed so that it could be accommodated on the synchrotron beamline. The replicator comprises a laser and optical system, a powder bed with a vibration assisted gravity-fed powder hopper, a blade-type spreader and a processing chamber with an argon flow and Kapton X-ray windows. A 1070 nm Ytterbium-doped fibre laser (SPI Lasers Ltd, UK) of 200 W laser power (P) was selected for the laser system. It operates in a continuous-wave (CW) mode. It is equipped with f-theta lens to focus its spot size down to with a $D4\sigma$ 50 μm with a symmetric Gaussian shape. The corresponding control system allows the scan speed (v) can reach 4 m s^{-1} . The actual scan speed was selected to enable a continuous track to be formed during laser melting. To adapt to X-ray imaging, a region of the powder bed 40 mm in width, 3 mm in height, and 0.3 mm in thickness were chosen (Supplementary Figure 1). It is positioned perpendicular to the X-ray beam and the laser beam (Fig. 1a). Two glassy carbon windows are fitted on the two sides of the CP-Ti substrate for complete transparency for the X-ray beam. Ti-6Al-4V powder (Supplementary Figure 2) is spread onto the substrate with hopper and the thickness is controlled with the motorised stage and blade spreader.

In this work, a commercially pure Ti substrate with dimensions of 46 mm in length and 0.3 mm in thickness in the x-ray direction was used as a substrate for the powder bed. The powder thickness of the first layer was controlled to be 100 μm and, after the melt-track was deposited the substrate was lowered by 100 μm and a new layer of powder was added. A schematic of the X-ray imaging process is shown in Figure 1a. Gas atomised Ti-6Al-4V powder was used in the experiments with a size range of 5 - 70 μm and a d_{50} (*median diameter*) of 45 μm (see Supplementary Figure 2). The powder bed is positioned inside the environmental build chamber which has X-ray windows and a flow of argon at 4 L min^{-1} is maintained throughout the experiment (see Supplementary). The scan speed was selected to be 100 mm s^{-1} to enable operating in keyhole mode with optimal imaging condition. In this operation condition, the laser powder density is 10.2 MW cm^{-2} which is above the threshold of $\sim 0.4 \text{ MW cm}^{-2}$ for keyhole mode operation²⁸.

09 A polychromatic beam was used for all trials with a peak X-ray energy of approximately 50 keV and a mean
10 energy of approximately 30 keV. The X-ray imaging system consisted of a 200 µm thick LuAg: Ce scintillator
11 and a 4× magnification long working distance objective lens (0.21 NA). The X-ray images was captured by a
12 Photron FASTCAM SA-Z 2100K at 40 kfps. This configuration provided an imaging resolution of
13 approximately 4.76 µm per pixel and an exposure time of 12.5 µs.

14 2.2 Image processing and quantification

15 We first apply a dark field correction in the Photron camera prior the image acquisition, and then we
16 processed all the acquired radiographs using ImageJ²⁹ and Matlab©. The acquired images are further
17 corrected to form a flat-field corrected (FFC) image by dividing by an average of 100 flat field images¹⁹.

18 The melt pool was segmented using Otsu's threshold method³⁰. And we used iterative PIV (Cross-correlation)
19 plugin³¹ from ImageJ to track the powder particles, melt flow and spatter (Details see Supplementary Figure
20 3). To increase the image contrast and signal-to-noise ratio, we applied a local-temporal background
21 subtraction to reveal key information in the X-ray images following equation:

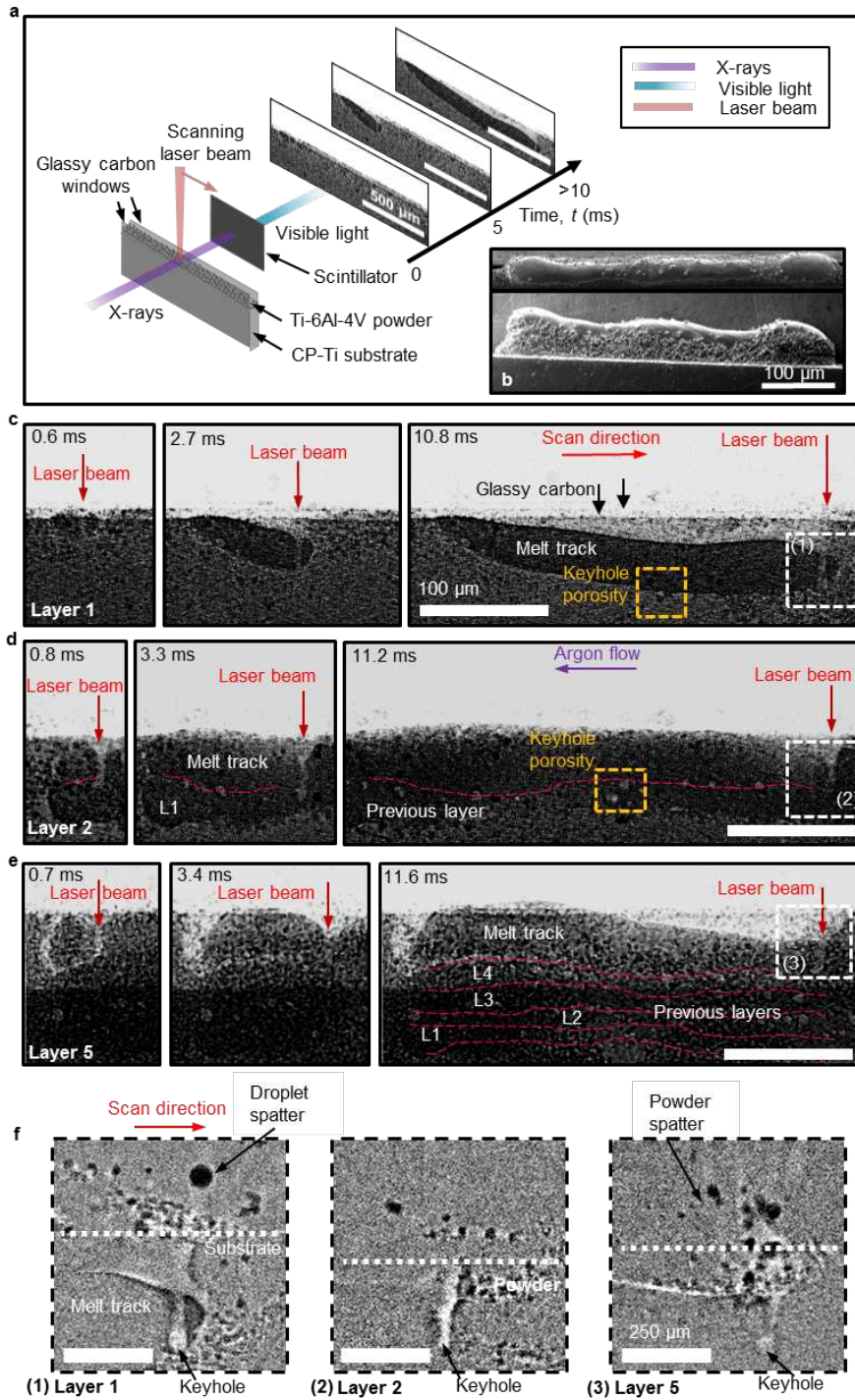
$$22 \quad \text{LTBS} = \frac{\text{FFC}}{I_{\text{avg}}} \quad (1)$$

23 Where LTBS is the local-temporal background subtracted image, *FFC* is the flat field corrected image, and
24 I_{avg} is a local average of 50 of the nearest neighbour images (25 before and 25 after).

25 3. Results & Discussion

26 3.1 Evolution of a multi-layer melt track during LPBF on a substrate plate

27 We performed *in situ* and operando X-ray imaging on the ID19 - Micro-tomography beamline at ESRF to
28 capture the transient phenomena during the LPBF of Ti-6Al-4V powder. The time-resolved evolution of the
29 morphology of each melt track in a multi-layer series of melt tracks was captured by the X-ray imaging during
30 laser melting and re-solidification (Fig. 1b and Supplementary Video 1).



31

32

33

34

35

36

37

38

39

40

41

42

Figure 1. Evolution of a multi-layer melt track during LAM on a substrate plate. (a) Schematic of the *in situ* and operando X-ray imaging of LPBF AM of Ti-6Al-4V. Scale bar = 500 μm . (b) Corresponding SEM images (top view and side view) of the multi-layer melt track built during the *in situ* and operando experiment. Scale bar = 100 μm . (c)-(e) Time-series radiographs acquired during LAM of a Ti-6Al-4V 100 μm melt track under $P = 200 \text{ W}$, $v = 100 \text{ mm s}^{-1}$ during layer 1, layer 2 & layer 5 of the build, respectively. Three radiographs were chosen for each layer of the build to indicate the initial, middle and final stage of the build in each track and the time since the build started is marked on each radiograph. The melt tracks were deposited in an alternating directional strategy but the radiographs were reversed to keep the building directions uniform and are from left to right in the images. A significant number of keyhole pores are found at the interface between the deposited layers. See Supplementary Video 1. Scale bar = 100 μm . (f) Enlarged view of the vapour depression area (filtered using local-temporal background subtraction) in the dotted boxes in Figure 1(c), (d) and (e). The melt pool appears in projection to be separated into two portions: ahead of and behind the laser beam induced key-hole. Droplet and powder spatter are ejected by the metal/gas vapour jet from the denuded zone with an angle near normal to the substrate surface. Scale bar = 250 μm .

43 The melt tracks were deposited in an alternating directional strategy up to 5 layers in height. Figure 1c-e
44 shows three images from the radiograph series taken from the start, middle and end of the deposition of the
45 first, the second and the fifth layers, respectively (see Supplementary Video 1). The laser beam was seen to
46 have consolidated powder particles into a continuous melt pool via laser melting and subsequent formation
47 of a solidified melt track. The use of a thin substrate had a side-effect in the first layer of build. The melt pool
48 touched the side wall, causing the surface of the melt-track to become depressed below the level of the
49 original substrate. At the point of laser-matter interaction the laser is shown to have created a deep vapour
50 depression, forming a keyhole throughout the melting process. Figure 1f provides an enlarged view of the
51 vapour depression area in Figure 1c-e. We applied local-temporal background subtraction (details see
52 methods section) to reveal the keyhole and spatter. Although one denuded (or powder free) zone surrounding
53 the laser beam was reported previously⁸ when observed from above, the radiographs showed that the melt
54 pool is in fact separated into two portions: ahead of and behind the laser beam induced keyhole. This
55 phenomenon was clearest in layer 1 as the image contrast between the melt pool and the substrate plate
56 was better than with the powder in subsequent layers.

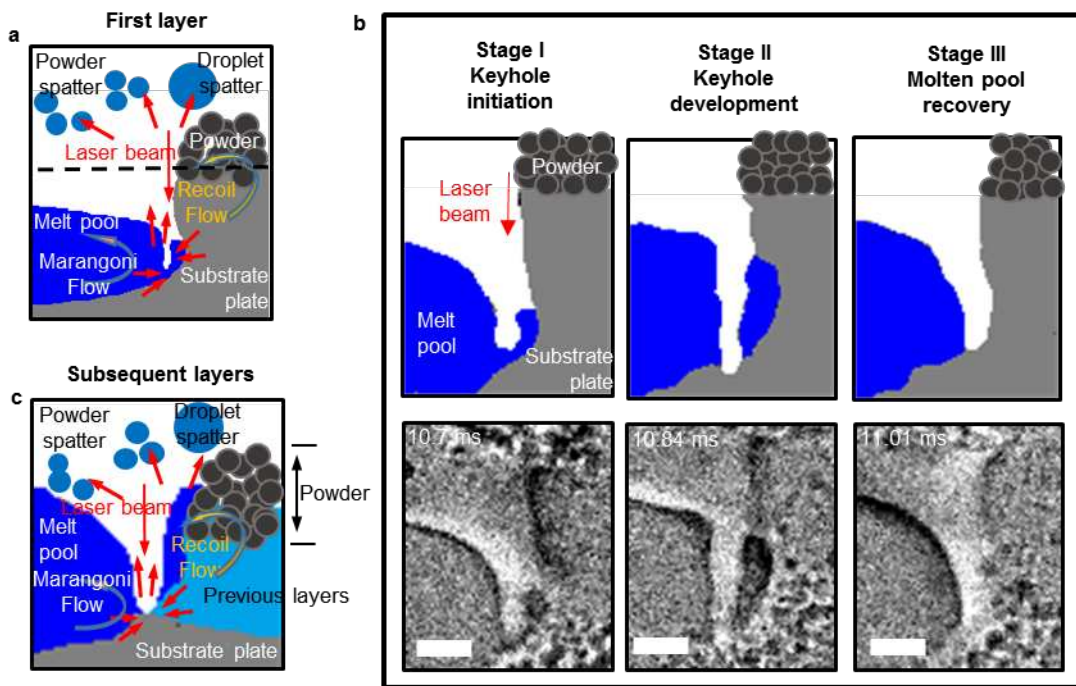
57 Most droplet and some powder spatter were ejected by the metal/gas vapour jet from the denuded zone
58 (powder-free zone) with most of the droplet spatter ejected with an angle near normal to the substrate surface.
59 We can distinguish whether spatter is droplet or powder by its diameter. Powder spatter had a diameter in
60 the range of powder particles ($\sim 45 \mu\text{m}$). Droplet spatter usually has a larger diameter ($> 100 \mu\text{m}$) which is a
61 molten droplet formed from powder agglomeration. Of the powder spatter, some ejected normal, but some
62 was observed to be ejected towards the melt track with a low angle.

63 Pores formed near the base of the keyhole and were apparently trapped by the fast-moving solidification
64 front, preventing them from rising upwards or escaping through the surface of the melt pool via Marangoni
65 convection. In this multi-layer build, the laser beam re-melted the previous layer whilst also consolidating
66 powder particles in the track. A significant number of pores was found at the interface between the deposited
67 layers (see Figure 1e – layer 5).

68 **3.2 Keyhole melt dynamics and related spatter formation mechanism**

69 A transient cyclic phenomenon of the keyhole melt pool dynamics was observed. (Figure 2 and
70 Supplementary Video 2 & 3). We employed particle tracking to track powder particles movements and infer

71 the fluid flow to elucidate melt pool dynamics and spatter formation. (Supplementary Figure 3) The dynamics
 72 of the keyhole melt pool can be defined as three stages. During Stage I, after a melt pool was formed at the
 73 start of the scan, the intense laser beam (power density of $\sim 10 \text{ MW m}^{-2}$) separated the melt pool and created
 74 a vapour depression (keyhole). The narrow keyhole channel was known to be the result of the vaporisation
 75 of the alloy and the multiple reflections of the laser beam on the keyhole walls¹³. The superheated vapour
 76 expanded and caused a high-velocity jet of gas normal to the substrate surface (estimated up to 700 m s^{-1})³²
 77 from the keyhole channel. Some of powder particles in the vicinity of the keyhole were ejected nearly normal
 78 to the substrate's surface with an average speed of 3 m s^{-1} as powder spatter (Supplementary Figure 4).



79

80 Figure 2. Melt pool dynamics revealed by X-ray imaging. (a) Schematics of the melt pool dynamics and spatter formation mechanisms in the first layer
 81 of build (See Supplementary Video 2). The melt pool is separated into two portions by the keyhole: ahead of and behind the laser beam. The
 82 Marangoni and recoil flow are contradictory and it caused a 'cut-off' of the melt flow underneath the vapour depression. Powder particles were being
 83 entrained into the melt-pool in the vicinity of the keyhole following the recoil flow and it formed molten droplets. Most droplet and some powder spatter
 84 are ejected by the metal/gas vapour jet from the denuded zone. (b) Schematics of the stages of the melt pool oscillation in the first layer. Three
 85 stages of melt pool dynamics were summarised as (I) Keyhole initiation, (II) Keyhole development, and (III) Molten pool recovery. The schematics
 86 were processed by image segmentation and the corresponding radiographs were revealed through local-temporal background subtraction. Scale bar
 87 = $100 \mu\text{m}$. (c) Schematics of the melt pool dynamics in the subsequent layers (The phenomenon see Supplementary Video 3). The phenomenon is
 88 similar to the first layer of build. Due to the re-melting of the previous layer, there was no distinctly visible melt bead in front of the laser, however, the
 89 elongated front melt pool was still visible which is formed by vapour driven powder entrainment.

90 In stage II, the high-velocity intense vapour jet in Stage I caused a pressure decrease inside the keyhole³³.
 91 As the high-velocity metal vapour jet propagated, it entrained argon gas and diverged. This induced a
 92 denudation zone³³ where powder particles were being entrained into the melt-pool in the vicinity of the
 93 keyhole following the recoil vapour flow and were engulfed into the front melt bead by capillary forces (see

94 Supplementary Video 2), creating a recoil flow. This is similar to the vapour-driven powder entrainment
95 observations reported previously when building takes place on loose powder³⁴.

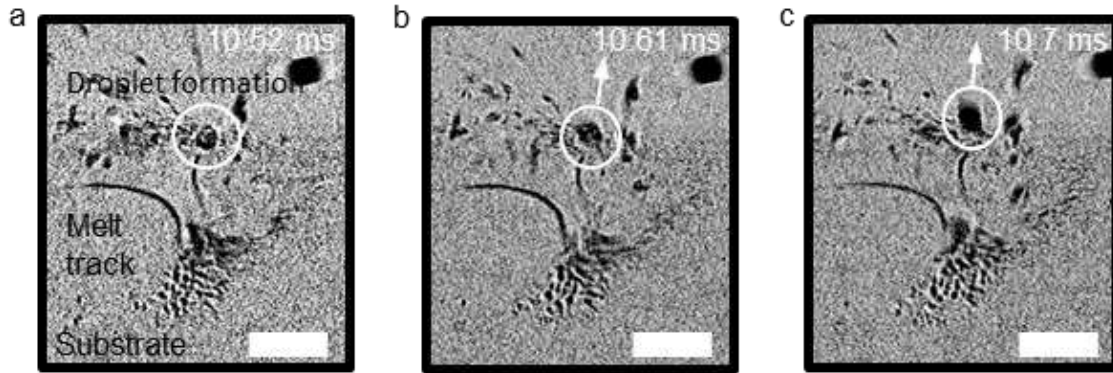
96 The Marangoni convection in the back portion of the melt pool is seen to be directed opposite to the building
97 direction³² and the recoil flow. As a result, it caused a temporary stall of the melt flow underneath the vapour
98 depression and allowed the laser beam to vaporise this stagnant region and 'cut-off' the portion of the melt
99 pool ahead of the laser (See Supplementary Video 2). Meanwhile, the melt bead in front of the laser increased
00 the volume due to the entrainment of powder particles. During which, the powder particles on the top
01 agglomerated by wetting and formed a molten droplet. These droplets were then entrained into the high
02 temperature metal vapour and increased the pressure in the keyhole leading to Stage III. This is when the
03 increase of keyhole pressure stabilized the keyhole and the front melt bead coalesced with the rear portion
04 via wetting (See Supplementary Video 2). The melt pool recovery in the first layer was about *ca.* 1 ms after
05 keyhole 'cut-off' in Stage II.

06 Overall, it is evident that the melt pool dynamics generated a perturbation of pressure in the vicinity of the
07 keyhole, leading to changes in keyhole morphology and droplet spatter ejection (Figure 3). The mechanism
08 is similar to that seen in the laser welding process described previously³⁵.

09 During Stage II of keyhole development in the first layer build, the projected keyhole was a narrow channel,
10 as seen in Figure 2. The decrease of vapour pressure at this moment enabled the powder particles to
11 agglomerate and to form droplet under recoil pressure without being ejected from the denudation zone (at
12 10.52 ms). During Stage III, Molten pool recovery, the keyhole opened up. Meanwhile, the vapour/gas jet
13 with an increased pressure carried the droplet out of the keyhole with an angle near normal to the substrate
14 surface (at 10.61 ms). The pressure in the keyhole then decreased before a new front melt pool is formed at
15 Stage I(at 10.70 ms). We observed that the phenomena was more drastic with an increase of powder layer
16 thickness. It indicated that an excess of powder particles was the main reason contributing to the pressure
17 variation.

18 A similar cyclic phenomenon of the keyhole melt dynamics was also found in subsequent layers of the build
19 (Supplementary Video 3). A vapour depression was formed on the previously built layer instead of the base
20 plate after a melt pool was formed. Due to the re-melting of the previous layer, although the elongated front
21 melt pool was still visible which was formed by vapour driven powder entrainment, the dynamic behaviour of

22 the melt pool was not as clear as in the first layer. Similar to the first layer build, the vapour-driven powder
23 entrainment enabled the front melt pool to increase its volume before it coalesced with the main melt pool.
24 We observed that the melt pool separation phenomenon repeats periodically throughout the whole laser
25 scanning process, revealing a new track formation mechanism (Supplementary Video 2) which is
26 summarised, into three stages: (I) keyhole initiation, (II) keyhole development, and (III) molten pool recovery.



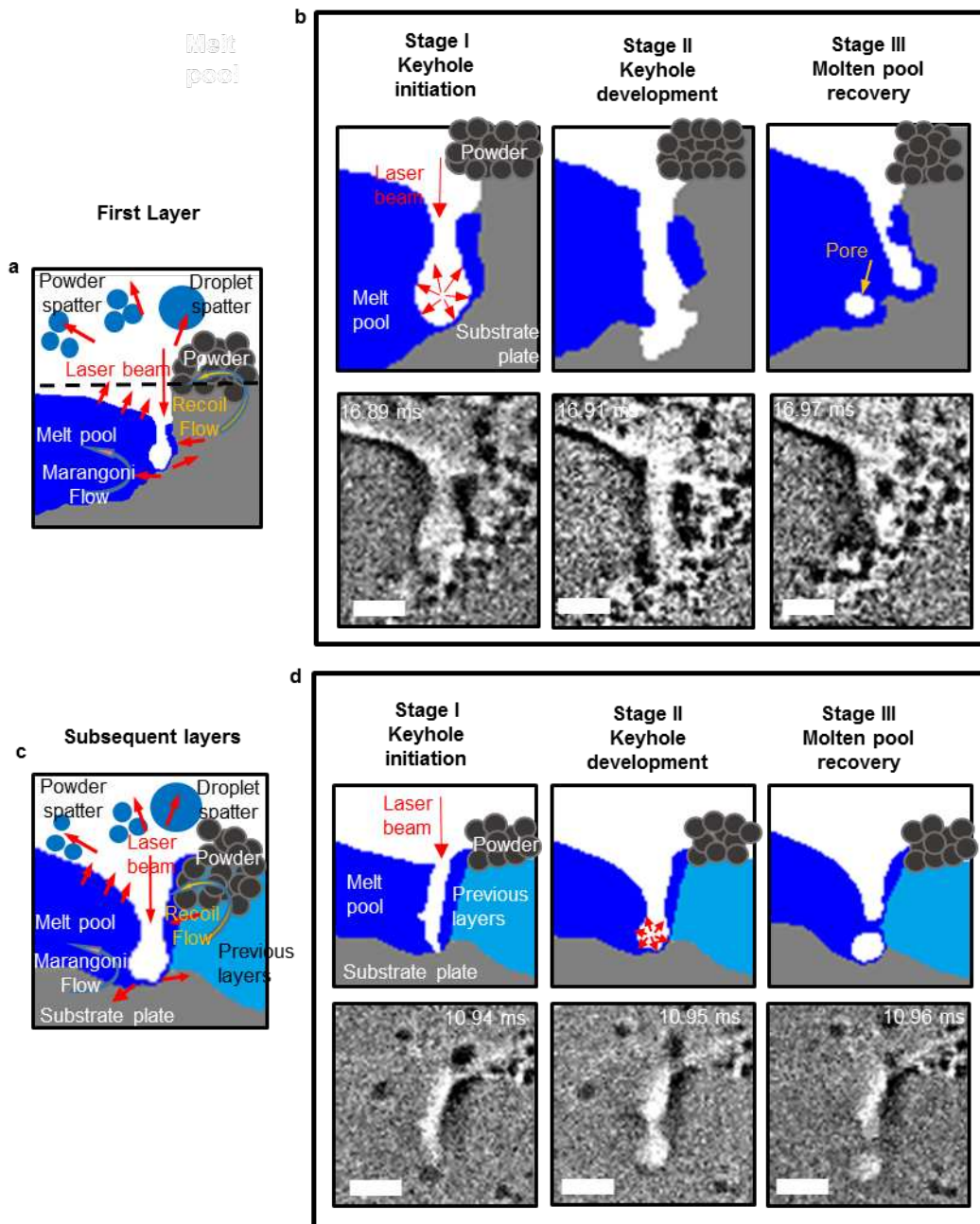
27

28 Figure 3. Time series of radiographs showing droplet spatter formation and its correlation with keyhole dynamics revealed through local-temporal
29 background subtraction on the first layer of build. Three radiographs were chosen to indicate (a) droplet formation by molten powder agglomeration
30 during Stage II Melt pool development, (b) droplet spatter ejection by the gas/vapour jet during Stage III Molten pool recovery, and (c) droplet spatter
31 been ejected while the melt pool started another cycle and returned to Stage I Melt pool initiation. The time since the build started is marked on each
32 radiograph. Scale bar = 250 μm .

33 3.3 Keyhole porosity formation mechanism

34 Keyhole porosity was observed to form during Stage II Melt pool development and Stage III Molten pool
35 recovery. Abundant interlayer porosity was observed during the multi-layer build and pores are found to be
36 introduced by the vapour depression. We employed particle tracking to reveal melt pool dynamics and spatter
37 formation (Figure 4) when keyhole porosity was formed.

38



39

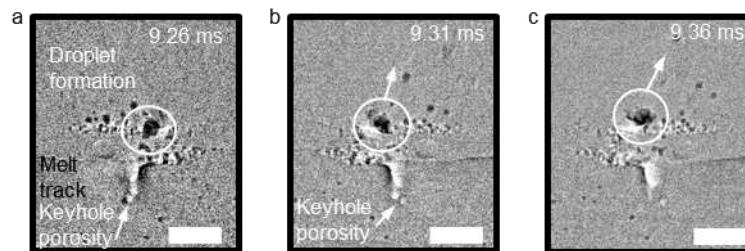
40 Figure 4. Keyhole porosity formation mechanism revealed by X-ray imaging. (a) Schematics of the phenomenon of keyhole pore formation in the first
 41 layer (See Supplementary Video 4). Similar to Figure 2(a), the melt pool was separated by the keyhole. The keyhole 'cut-off' was due to the rapid
 42 gas/vapour expansion inside the keyhole. Most droplet and some powder spatter are ejected by the metal/gas vapour jet from the denuded zone. (b)
 43 Schematics of the stages of the melt pool oscillation in the first layer. The three stages of melt pool dynamics are summarised as (I) Keyhole initiation,
 44 (II) Keyhole development, and (III) Molten pool recovery. The laser-induced gas/vapour was then entrained into the melt track below the keyhole and
 45 formed a keyhole pore. The schematics were processed by image segmentation and the corresponding radiographs were revealed through local-
 46 temporal background subtraction. Scale bar = 100 μm . (c) Schematics of keyhole pore formation phenomenon in the subsequent layers (See
 47 Supplementary Video 5). The phenomenon is similar to the first layer of build with a clear keyhole porosity formed in the melt track. (d) Schematics
 48 of the melt pool oscillation during keyhole pore formation in the subsequent layers. Three stages of melt pool dynamics were also summarised that
 49 matched with the first layer. Scale bar = 100 μm .

50 We hypothesise that in regions where the packing density³⁶ is locally reduced, more metal vapour is
 51 generated. This is due to a combination of the changes of surface contact area and the effective absorption
 52 and thermal conductivity from a looser powder layer. Lower packing density introduced higher local laser-

53 powder interaction surface area, and it increased the local laser energy absorption, and thus increased the
54 vaporization rate. We further hypothesise that when the powder packing density³⁶ varies along the laser scan
55 path, more metal vapour was generated, compared to even powder packing density. Along with sufficient
56 ambient argon gas, it caused a rapid gas/vapour expansion inside the keyhole during Stage I Keyhole
57 initiation. The gas/vapour expansion rapidly pushed the molten liquid around it, causing a 'cut-off' of the melt
58 pool as in Stage II Keyhole development. As the result, the laser-induced gas/vapour was then been
59 entrained into the melt track below the keyhole and formed a keyhole pore during Stage III Molten pool
60 recovery (Supplementary Video 4). Similarly, in the subsequent layers of build, the rapid gas/vapour
61 expansion in Stage I created a 'cut-off' of the melt pool in Stage II. The gas/vapour was then been entrained
62 beneath the keyhole during Stage III and formed a keyhole porosity (Supplementary Video 5).

63 **3.4 Spatter formation mechanism correlated with keyhole porosity**

64 The drastic cyclic oscillation of the melt pool generated a recoil pressure which promotes spatter to be ejected
65 out of the denudation zone as shown in Figures 1, 2, 3 and 4. Some powder spatter was ejected at a low
66 angle with respect to the substrate surface plane. Meanwhile, the stronger gas/vapour jet from Stage II during
67 keyhole porosity formation enabled agglomerated molten droplets to be carried out nearly vertically at an
68 average speed of 2.2 m s^{-1} as droplet spatter, as shown in Figure 5 and Supplementary Video 6.



69
70 Figure 5. Time series of radiographs showing droplet spatter formation is associated with the cyclical melt pool dynamics and has a strong correlation
71 with keyhole pore formation revealed through local-temporal background subtraction on the subsequent layer of the build. See Supplementary Video
72 6. Three radiographs were chosen to indicate (a) droplet formation by molten powder agglomeration during Stage II Melt pool development when a
73 keyhole porosity was forming, (b) droplet spatter ejection by gas/vapour jet during Stage III Molten pool recovery when a keyhole porosity was formed,
74 and (c) droplet spatter been ejected out while the melt pool started another cycle and back to Stage I Melt pool initiation. A keyhole porosity can be
75 observed in the melt track. The time since the build started was marked on each radiograph. Scale bar = $250 \mu\text{m}$.

76 The dominant formation mechanism for a molten droplet is the agglomeration of molten powder particles
77 induced by the recoil pressure³⁷ during Stage II melt pool development. However, whether the molten droplet
78 can be ejected as droplet spatter depends on the pressure of the vaporised gas flow from the keyhole. As
79 we have observed, the agglomerated droplets can dissipate into the keyhole due to the lack of a sufficiently

80 strong vapour jet when keyhole porosity did not occur. We also hypothesize that droplet spatter ejection is
81 correlated with the formation of keyhole porosity during which a higher vapour pressure is generated. This
82 phenomenon occurred in both the first layer and in the subsequent layers of the build.

83 **Conclusions**

84 We have used in situ and operando synchrotron X-ray imaging to uncover the key mechanisms of multi-layer
85 LPBF of Ti-6Al-4V operating in keyhole mode. We revealed the underlying mechanisms of melt pool and
86 keyhole dynamics and how this affected the mechanisms of porosity and spatter formation in multi-layer
87 conditions. For the first time, we observed that melt pool separation and cyclic melt track evolution occurred
88 during the building of 5 successive layers of Ti6Al4V. The melt pool oscillation involves three stages of
89 evolution: (I) keyhole initiation, (II) keyhole development, and (III) melt pool recovery. We also elucidated
90 both porosity and spatter formation mechanisms during the keyhole oscillation. Keyhole porosity was
91 observed to form during the transient (I) keyhole initiation stage when the melt pool splits. Droplet spatter
92 formation was directly correlated with the melt pool recovery stage by the agglomeration and subsequent
93 ejection of powder particles introduced by recoil pressure in the denudation zone. The keyhole-related
94 phenomena in a multilayer build were found to similar in all layers. Our results clarified the physics behind
95 keyhole mode LPBF and can be coupled with modelling to improve the quality of LPBF built components.
96 The mechanisms observed are applicable to more materials processing techniques such as laser welding
97 and electron beam additive manufacturing where keyhole mode porosity and excessive spatter needed to be
98 avoided.

99 **Acknowledgement**

00 The authors acknowledge financial support from MAPP: EPSRC Future Manufacturing Hub in Manufacture
01 using Advanced Powder Processes (EP/P006566/1) and a Royal Academy of Engineering Chair in Emerging
02 Technology, and Rolls-Royce plc. via the Horizon 2020 Clean Sky 2 WP5.8.1 programmes (YC) and through
03 support of LS's studentship. We also acknowledge the use of facilities and support provided by the Research
04 Complex at Harwell and thank the ESRF for providing the beam-time proposal (no: MA4061) and staff at
05 ID19 beamline for technical assistance. The authors also thank Professor Graham McCartney for reading
06 through the manuscript. We thank Photron Ltd. for providing the high-speed camera (FASTCAM SAZ 2100K)

07 to perform this experiment. We'd also acknowledge Dr. Samuel McDonald and Dr. Sam Tammam-Williams
08 for their assistance during this beam time.

09 **Author contribution**

10 P.D.L. conceived the project. C.L.A.L. and S.M., led the design of the *In Situ and Operando* Powder bed
11 process Replicator (ISOPR). C.L.A.L and Y.C. designed and performed the experiments, with all authors
12 contributing. Y.C. performed the data analysis with S.C contributing. Y.C and P.D.L. led the results
13 interpretation and paper writing, with all authors contributing.

14 **References:**

- 15 1. Tan Phuc, L. & Seita, M. A high-resolution and large field-of-view scanner for in-line characterization
16 of powder bed defects during additive manufacturing. *Mater. Des.* **164**, 107562 (2019).
- 17 2. Wang, Y. *et al.* Probing deformation mechanisms of a FeCoCrNi high-entropy alloy at 293 and 77 K
18 using in situ neutron diffraction. *Acta Mater.* **154**, 79–89 (2018).
- 19 3. Rometsch, P., Jia, Q., V. Yang, K. & Wu, X. Aluminum alloys for selective laser melting – towards
20 improved performance. *Addit. Manuf. Aerosp. Ind.* 301–325 (2019). doi:10.1016/B978-0-12-814062-
21 8.00016-9
- 22 4. Soro, N., Attar, H., Wu, X. & Dargusch, M. S. Investigation of the structure and mechanical
23 properties of additively manufactured Ti-6Al-4V biomedical scaffolds designed with a Schwartz
24 primitive unit-cell. *Mater. Sci. Eng. A* **745**, 195–202 (2019).
- 25 5. Nommeots-Nomm, A. *et al.* Four-dimensional imaging and quantification of viscous flow sintering
26 within a 3D printed bioactive glass scaffold using synchrotron X-ray tomography. *Mater. Today Adv.*
27 **2**, 100011 (2019).
- 28 6. Zhakeyev, A. *et al.* Additive Manufacturing: Unlocking the Evolution of Energy Materials. *Adv. Sci.* **4**,
29 (2017).
- 30 7. Yufit, V. *et al.* Operando Visualization and Multi-scale Tomography Studies of Dendrite Formation
31 and Dissolution in Zinc Batteries. *Joule* **3**, 485–502 (2019).
- 32 8. Matthews, M. J. *et al.* Denudation of metal powder layers in laser powder bed fusion processes. *Acta*

- 33 *Mater.* **114**, 33–42 (2016).
- 34 9. Choo, H. *et al.* Effect of laser power on defect, texture, and microstructure of a laser powder bed
35 fusion processed 316L stainless steel. *Mater. Des.* **164**, 107534 (2019).
- 36 10. Guo, Q. *et al.* Transient dynamics of powder spattering in laser powder bed fusion additive
37 manufacturing process revealed by in-situ high-speed high-energy x-ray imaging. *Acta Mater.* **151**,
38 169–180 (2018).
- 39 11. Rai, R., Elmer, J. W., Palmer, T. A. & Debroy, T. Heat transfer and fluid flow during keyhole mode
40 laser welding of tantalum, Ti-6Al-4V, 304L stainless steel and vanadium. *J. Phys. D: Appl. Phys.* **40**,
41 5753–5766 (2007).
- 42 12. Fabbro, R. Scaling laws for the laser welding process in keyhole mode. *J. Mater. Process. Technol.*
43 **264**, 346–351 (2019).
- 44 13. Dai, D. & Gu, D. Effect of metal vaporization behavior on keyhole-mode surface morphology of
45 selective laser melted composites using different protective atmospheres. *Appl. Surf. Sci.* **355**, 310–
46 319 (2015).
- 47 14. King, W. E. *et al.* Observation of keyhole-mode laser melting in laser powder-bed fusion additive
48 manufacturing. *J. Mater. Process. Technol.* **214**, 2915–2925 (2014).
- 49 15. Liu, Y., Yang, Y., Mai, S., Wang, D. & Song, C. Investigation into spatter behavior during selective
50 laser melting of AISI 316L stainless steel powder. *Mater. Des.* **87**, 797–806 (2015).
- 51 16. Everton, S. K., Hirsch, M., Stravroulakis, P., Leach, R. K. & Clare, A. T. Review of in-situ process
52 monitoring and in-situ metrology for metal additive manufacturing. *Mater. Des.* **95**, 431–445 (2016).
- 53 17. Qiu, C. *et al.* On the role of melt flow into the surface structure and porosity development during
54 selective laser melting. *Acta Mater.* **96**, 72–79 (2015).
- 55 18. Leung, C. L. A. *et al.* Laser-matter interactions in additive manufacturing of stainless steel SS316L
56 and 13-93 bioactive glass revealed by in situ X-ray imaging. *Addit. Manuf.* **24**, 647–657 (2018).
- 57 19. Leung, C. L. A. *et al.* In situ X-ray imaging of defect and molten pool dynamics in laser additive
58 manufacturing. *Nat. Commun.* **9**, 1–9 (2018).

- 59 20. Materlik, G., Rayment, T. & Stuart, D. I. Diamond Light Source: Status and perspectives. *Philos.*
60 *Trans. R. Soc. A Math. Phys. Eng. Sci.* **373**, (2015).
- 61 21. Drakopoulos, M. *et al.* I12: The Joint Engineering, Environment and Processing (JEEP) beamline at
62 Diamond Light Source. *J. Synchrotron Radiat.* **22**, 828–838 (2015).
- 63 22. Cunningham, R. *et al.* Keyhole threshold and morphology in laser melting revealed by ultrahigh-
64 speed x-ray imaging. *Science (80-.)*. **363**, 849–852 (2019).
- 65 23. Kouraytem, N. *et al.* Effect of Laser-Matter Interaction on Molten Pool Flow and Keyhole Dynamics.
66 *Phys. Rev. Appl.* **11**, 1 (2019).
- 67 24. Hojjatzadeh, S. M. H. *et al.* Pore elimination mechanisms during 3D printing of metals. *Nat.*
68 *Commun.* **10**, 1–8 (2019).
- 69 25. Martin, A. A. *et al.* Dynamics of pore formation during laser powder bed fusion additive
70 manufacturing. *Nat. Commun.* **10**, 1–10 (2019).
- 71 26. Guo, Q. *et al.* Transient dynamics of powder spattering in laser powder bed fusion additive
72 manufacturing process revealed by in-situ high-speed high-energy x-ray imaging. *Acta Mater.* **151**,
73 169–180 (2018).
- 74 27. Zhao, C. *et al.* Bulk-Explosion-Induced Metal Spattering During Laser Processing. *Phys. Rev. X* **9**,
75 21052 (2019).
- 76 28. Cunningham, R., Zhao, C., Parab, N. & Kantzos, C. Keyhole threshold and morphology in laser
77 melting revealed by ultrahigh-speed x-ray imaging. **852**, 849–852 (2019).
- 78 29. Schindelin, J. *et al.* Fiji: an open-source platform for biological-image analysis. *Nat. Methods* **9**, 676–
79 682 (2012).
- 80 30. Smith, P. *et al.* Otsu_1979_otsu_method. **C**, 62–66 (1979).
- 81 31. Tseng, Q. *et al.* Spatial organization of the extracellular matrix regulates cell-cell junction positioning.
82 *Proc. Natl. Acad. Sci. U. S. A.* **109**, 1506–1511 (2012).
- 83 32. Bidare, P., Bitharas, I., Ward, R. M., Attallah, M. M. & Moore, A. J. Fluid and particle dynamics in
84 laser powder bed fusion. *Acta Mater.* **142**, 107–120 (2018).

- 85 33. Matthews, M. J. *et al.* Denudation of metal powder layers in laser powder bed fusion processes. *Acta*
86 *Mater.* **114**, 33–42 (2016).
- 87 34. Leung, C. L. A. *et al.* The effect of powder oxidation on defect formation in laser additive
88 manufacturing. *Acta Mater.* (2018). doi:10.1016/J.ACTAMAT.2018.12.027
- 89 35. Ly, S., Rubenchik, A. M., Khairallah, S. A., Guss, G. & Matthews, M. J. Metal vapor micro-jet controls
90 material redistribution in laser powder bed fusion additive manufacturing. *Sci. Rep.* **7**, 1–12 (2017).
- 91 36. Choi, J.-P. *et al.* Evaluation of Powder Layer Density for the Selective Laser Melting (SLM) Process.
92 *Mater. Trans.* **58**, 294–297 (2017).
- 93 37. Khairallah, S. A., Anderson, A. T., Rubenchik, A. & King, W. E. Laser powder-bed fusion additive
94 manufacturing: Physics of complex melt flow and formation mechanisms of pores, spatter, and
95 denudation zones. *Acta Mater.* **108**, 36–45 (2016).

96